1 # Deep Ocean Temperatures through Time

2 Paul J Valdes[1], Christopher R Scotese[2], Daniel J Lunt[1]

4 [1] School of Geographical Sciences, University of Bristol, Bristol BS8 1SS, UK

5 [2] Northwestern University, Dept Earth & Planetary Sci, Evanston, IL USA

6 Correspondence to: Paul Valdes (P.J.Valdes@bristol.ac.uk)

7 ## Abstract

8 Benthic oxygen isotope records are commonly used as a proxy for global mean surface temperatures

9 during the late Cretaceous and Cenozoic, and the resulting estimates have been extensively used in

10 characterising major trends and transitions in the climate system, and for analysing past climate

11 sensitivity. However, some fundamental assumptions governing this proxy have rarely been tested.

12 Two key assumptions are: (a) benthic foraminiferal temperatures are geographically well mixed and

13 are linked to surface high latitude temperatures, and (b) surface high latitude temperatures are well

14 correlated with global mean temperatures. To investigate the robustness of these assumptions

15 through geological time, we performed a series of 109 climate model simulations using a unique set

16 of paleogeographical reconstructions covering the entire Phanerozoic at the stage-level. The

17 simulations have been run for at least 5000 model years to ensure that the deep ocean is in dynamic

18 equilibrium. We find that the correlation between deep ocean temperatures and global mean

19 surface temperatures is good for the Cenozoic and thus the proxy data are reliable indicators for this

20 time period, albeit with a standard error of 2K. This uncertainty has not normally been assessed and

21 needs to be combined with other sources of uncertainty when, for instance, estimating climate

22 sensitivity based on using $\delta^{18}O$ measurements from benthic foraminifera. The correlation between

23 deep and global mean surface temperature becomes weaker for pre-Cenozoic time periods (when

24 the paleogeography is significantly different than the present-day). The reasons for the weaker

25 correlation includes variability in the source region of the deep water (varying hemispheres but also

26 varying latitudes of sinking), the depth of ocean overturning (some extreme warm climates have

27 relatively shallow and sluggish circulations weakening the link between surface and deep ocean),

28 and the extent of polar amplification (e.g. ice albedo feedbacks). Deep ocean sediments prior to the

29 Cretaceous are rare, so extending the benthic foram proxy further into deeper time is problematic,

30 but the model results presented here would suggest that the predicted deep ocean temperatures

31 would probably be unreliable.

1. Introduction

One of the most widely used proxies for estimating global mean surface temperature through the last 100 million years is benthic $\delta^{18}O$ measurements from deep sea foraminifera (Zachos et al., 2001), (Zachos et al., 2008), (Cramer et al., 2009), (Friedrich et al., 2012). Two key underlying assumptions are that $\delta^{18}O$ from benthic foraminifera represents deep ocean temperature (with a correction for ice volume effects and any vital effects), and that the deep ocean water masses originate from surface water in polar regions. By further assuming that polar surface temperatures are well correlated with global mean surface temperatures, then deep ocean isotopes can be assumed to track global mean surface temperatures. More specifically, (Hansen et al., 2008), and (Hansen and Sato, 2012) argue that changes in high latitude sea surface temperatures are approximately proportional to global mean surface temperatures because changes are generally amplified at high latitudes but that this is offset because temperature change is amplified over land areas. They therefore equate changes in benthic ocean temperatures with global mean surface temperature.

The resulting estimates of global mean surface air temperature have been used to understand past climates (e.g. (Zachos et al., 2008)). Combined with estimates of atmospheric CO_2 they have also been used to estimate climate sensitivity (e.g. (Hansen et al., 2013)) and hence contribute to the important ongoing debate about the likely magnitude of future climate change.

However, some of the underlying assumptions behind the method remains largely untested, even though we know that there are major changes to paleogeography and consequent changes in ocean circulation and location of deep-water formation in the deep past (e.g. (Lunt et al., 2010; Nunes and Norris, 2006); (Farnsworth et al., 2019a)). Moreover, the magnitude of polar amplification is likely to vary depending on the extent of polar ice caps, and changes in cloud cover (Sagoo et al., 2013), (Zhu et al., 2019). These issues are likely to modify the correlation between deep ocean temperatures and global mean surface temperature or, at the very least, increase the uncertainty in reconstructing past global mean surface temperatures.

The aim of this paper is to investigate the strength and accuracy of the deep ocean temperature proxy using a unique set of 109 climate model simulations of the whole Phanerozoic era (last 540 million years) at the stage level (approximately every 5 million years). We use this set of model simulations to study the relationship between deep ocean temperature and global mean surface temperature.

65 The focus of the work is to examine the mechanisms that link benthic ocean temperatures and

66 surface conditions. However, we evaluate the fidelity of the model by comparing the model

67 predicted ocean temperatures to estimates of the isotopic temperature of the deep ocean during

68 the past 110 million years ((Zachos et al., 2008), (Cramer et al., 2009), (Friedrich et al., 2012)), and

69 model predicted surface temperatures to the sea surface temperatures estimates of (O'Brien et al.,

70 2017) and (Cramwinckel et al., 2018). This gives us confidence that the model is behaving plausibly.

71 We then use the complete suite of climate simulations to examine changes in ocean circulation, ice

72 formation, and the impact on ocean and surface temperature. Our paper will not consider any issues

73 associated with assumptions regarding the relationship between deep-sea foraminifera $\delta^{18}O$ and

74 various temperature calibrations because our model does not simulate the $\delta^{18}O$ of sea water (or

75 vital effects).

76

2. Simulation Methodology

2.1 Model Description

79 We use a variant of the Hadley Centre model, HadCM3 ((Pope et al., 2000), (Gordon et al., 2000))

80 which is a coupled atmosphere-ocean-vegetation model. The specific version, HadCM3BL-M2.1Da, is

81 described in detail in (Valdes et al., 2017). The model has a horizontal resolution of 3.75° x 2.5° in

82 longitude/latitude (roughly corresponding to an average grid box size of ~300km) in both the

83 atmosphere and the ocean. The atmosphere has 19 unequally spaced vertical levels, and the ocean

84 has 20 unequally spaced vertical levels. Though HadCM3 is relatively low resolution and complexity

85 model compared to the current CMIP5/CMIP6 state-of-the-art model, its performance at simulating

86 modern climate is comparable to many CMIP5 models (Valdes et al., 2017).

87 In order to perform paleo simulations, several important modifications to the standard model

88 described in (Valdes et al., 2017) must be incorporated:

89 (a) The standard pre-industrial model uses a prescribed climatological pre-industrial ozone

90   concentration (i.e. prior to the development of the "ozone" hole) which is a function of

91   latitude, atmospheric height and month of the year. However, we do not know what the

92   distribution of ozone should be in these past climates. (Beerling et al., 2011) modelled small

93   changes in tropospheric ozone for the early Eocene and Cretaceous but no comprehensive

94   stratospheric estimates are available. Hence most paleoclimate model simulations assume

95   unchanging concentrations. However, there is a problem with using a prescribed ozone

96   distribution for paleo simulations because it does not incorporate ozone feedbacks

97   associated with changes in tropospheric height. During warm climates, the model predicts

98   that the tropopause would rise. In the real world, ozone would track the tropopause rise,

99   however, this rising ozone feedback is not included in our model. This leads to substantial

100   extra warming and artificially increases the apparent climate sensitivity. Simulations of

101   future climate change have shown that ozone feedbacks can lead to an over-estimate of

102   climate sensitivity by up to 20% ((Dietmuller et al., 2014), (Nowack et al., 2015)). Therefore,

103   in order to incorporate some aspects of this feedback, we have changed the ozone scheme

104   in the model. Ozone is coupled to the model predicted tropopause height every model

105   timestep in the following simple way:

106   • 2.0×10^{-8} kg/kg in the troposphere

107   • 2.0×10^{-7} kg/kg at the tropopause

108   • 5.5×10^{-6} kg/kg above the tropopause

109   • 5.5×10^{-6} kg/kg at the top model level.

110   These values are approximate averages of present-day values and were chosen so that the

111   tropospheric climate of the resulting pre-industrial simulation was little altered compared

112   with the standard preindustrial simulations; the resulting global mean surface air

113   temperatures differed by only 0.05 ˚C. These modifications are similar to those used in the

114   FAMOUS model (Smith et al., 2008) except that the values in the stratosphere are greater in

115   our simulation, largely because our model vertical resolution is higher than in FAMOUS.

116   Note that these changes improve upon the scheme used by (Lunt et al., 2016). They used

117   much lower values of stratospheric ozone and had no specified value at the top of the

118   model. This resulted in their model having ~ 1˚C cold bias for pre-industrial temperatures.

119   This may have also affected their estimates of climate sensitivity.

120   (b) The standard version of HadCM3 conserves the total volume of water throughout the

121   atmosphere and ocean (including in the numerical scheme) but several processes in the

122   model "lose or gain" water

123   1.   Snow accumulates over ice sheets but there is no interactive loss through iceberg

124   calving resulting in an excess loss of fresh water from the ocean.

125   2.   The model caps salinity at a maximum of 45 PSU (and a minimum of 0 PSU), by

126   artificially adding/subtracting fresh water to the ocean. This mostly affects small

127   enclosed seas (such as the Red Sea or enclosed Arctic) where the model does not

128   represent the exchanges with other ocean basins.

3. Modelled river runoff includes some river basins which drain internally. These often correspond to relatively dry regions, but any internal drainage simply disappears from the model.

4. The land surface scheme includes evaporation from sub-grid scale lakes (which are prescribed as a lake fraction in each grid box, at the start of the run). The model does not represent the hydrological balance of these lakes, consequently the volume of the lakes does not change. This effectively means that there is a net source/sink of water in the model in these regions.

In the standard model, these water sources/sinks are approximately balanced by a flux of water into the surface ocean. This is prescribed at the start of the run and does not vary during the simulations. It is normally set to a pre-calculated estimate based on an old HadCM3-M1 simulation. The flux is strongest around Greenland and Antarctica and is chosen such that it approximately balances the water loss described in (1) i.e. the net snow accumulation over these ice sheets. There is an additional flux covering the rest of the surface ocean which approximately balances the water loss from the remaining three terms (2-4). The addition of this water flux keeps the global mean ocean salinity approximately constant on century time scales. However, depending on the simulation the drift in average oceanic salinity can be as much as 1PSU per thousand years and thus can have a major impact on ultra-long runs ((Farnsworth et al., 2019a).

For the paleo-simulations in this paper, we therefore take a slightly different approach. When ice sheets are present in the Cenozoic, we include the water flux (for the relevant hemisphere) described in (1) above, based on modern values of iceberg calving fluxes for each hemisphere. However, to ensure that salinity is conserved, we also interactively calculate an additional globally uniform surface water flux based on relaxing the volume mean ocean salinity to a prescribed value on a 20-year timescale. This ensures that there is no long-term trend in ocean salinity. Tests of this update on the pre-industrial simulations revealed no appreciable impact on the skill of the model relative to the observations.

2.2 Model Boundary Conditions

There are several boundary conditions that require modification through time. In this sequence of simulations, we only modify three key time-dependent boundary conditions: 1) the solar constant, 2) atmospheric CO_2 concentrations and, 3) paleogeographic reconstructions. We set the surface soil

161   conditions to a uniform medium loam everywhere. All other boundary conditions (such as orbital

162   parameters, volcanic aerosol concentrations etc.) are held constant at pre-industrial values.

163   The solar constant is based on (Gough, 1981) and increases linearly at an approximate rate of 11.1

164   Wm^{-2} per 100 Ma (0.8% per 100Ma), to 1365Wm^{-2} currently. If we assume a planetary albedo of 0.3,

165   and a climate sensitivity of 0.8 ˚C /Wm^{-2} (equivalent to 3˚C per doubling of CO_2), then this is

166   equivalent to a temperature increase of ~.015˚C per million years (8.1˚C over the whole of the

167   Phanerozoic).

168   Estimates of atmospheric CO_2 concentrations have considerable uncertainty. We, therefore, use two

169   alternative estimates (fig. 1a). The first uses the best fit Loess curve from (Foster et al., 2017), which

170   is also very similar to the newer data from (Witkowski et al., 2018). The CO_2 levels have considerable

171   short and long-term variability throughout the time period. The second curve removes much of the

172   shorter term variability in the Foster (2017) curve. It was used for two reasons. Firstly, a lot of the

173   finer temporal structure in the Loess curve is a product of different sampling numbers of the raw

174   data and does not necessarily correspond to real features. Secondly, the smoother curve was heavily

175   influenced by a previous (commercially confidential) sparser sequence of simulations using non-

176   public paleogeographic reconstructions and which were in good agreement with terrestrial proxy

177   datasets (Harris et al., 2017). The first-order shapes of the two curves are similar, though they are

178   very different for some time periods (e.g. Triassic and Jurassic). Both curves largely sit within the

179   range of actual data points. We refer to the simulation using the second set of CO_2 reconstructions

180   as the "smooth" CO_2 simulations, though it should be recognised that the Foster CO_2 curve has also

181   been smoothed. The Foster CO_2 curve extends only back to 420 Ma, so we have proposed two

182   alternative extensions back to 540 Ma. Both curves increase sharply so that the combined forcing of

183   CO_2 and solar constant are approximately constant over this time period (Foster et al., 2017). The

184   higher CO_2 in the Foster curve relative to the "smooth" curve is because the initial set of simulations

185   showed that the Cambrian simulations were relatively cool compared to data estimates for the

186   period (Henkes et al., 2018).

187   2.3 Paleogeographic Reconstructions

188   The 109 paleogeographic maps used in the HadleyCM3 simulations are digital representations of the

189   maps in the PALEOMAP Paleogeographic Atlas (Scotese, 2016); (Scotese and Wright, 2018). Table 1

190   lists all the time intervals that comprise the PALEOMAP Paleogeographic Atlas. The PaleoAtlas

191   contains one map for nearly every stage in the Phanerozoic. A paleogeographic map is defined as a

192   map that shows the ancient configuration of the ocean basins and continents, as well as important

193   topographic and bathymetric features such as mountains, lowlands, shallow sea, continental

194   shelves, and deep oceans.

195   Once the paleogeography for each time interval has been mapped, this information is then

196   converted into a digital representation of the paleotopography and paleobathymetry. Each digital

197   paleogeographic model is composed of over 6 million grid cells that capture digital elevation

198   information at a 10 km x 10 km horizontal resolution and 40-meter vertical resolution. This

199   quantitative, paleo-digital elevation model, or "paleoDEM", allows us to visualize and analyze the

200   changing surface of the Earth through time using GIS software and other computer modeling

201   techniques. For use with the HadCM3L climate model, the original high-resolution elevation grid was

202   reduced to a ~111 km x ~111 km (1˚ x 1˚) grid.

203   For a detailed description of how the paleogeographic maps and paleoDEMs were produced the

204   reader is referred to (Scotese, 2016); (Scotese and Schettino, 2017); (Scotese and Wright, 2018).

205   (Scotese and Schettino, 2017) includes an annotated bibliography of the more than 100 key sources

206   of paleogeographic information.   Similar paleogeographic paleoDEMs have been produced by

207   (Baatsen et al., 2016) and (Verard et al., 2015).

208   The raw paleogeographic data reconstructs paleo-elevations and paleo-bathymetry at a resolution of

209   1º x 1º. These data were re-gridded to 3.75º x 2.5º resolution that matched the GCM using a simple

210   area (for land sea mask) or volume (for orography and bathymetry) conserving algorithm. The

211   bathymetry was lightly smoothed (using a binomial filter) to ensure that the ocean properties were

212   numerically stable. The high latitudes had this filter applied multiple times. The gridding sometimes

213   produced single grid point enclosed ocean basins, particularly along complicated coastlines, and

214   these were manually removed. Similarly, important ocean gateways were reviewed to ensure that

215   the re-gridded coastlines preserved these structures. The resulting global fraction of land is

216   summarized in fig.1b and examples are shown in figure 2. The original reconstructions can be found

217   at https://www.earthbyte.org/paleodem-resource-scotese-and-wright-2018/

218   The paleogeographic reconstructions also include an estimate of land ice area ((Scotese and Wright,

219   2018); fig.1c). These were converted to GCM boundary conditions assuming a simple parabolic

220   shape to estimate the ice sheet height. Unlike (Lunt et al., 2016), these ice reconstructions suggest

221   small amounts of land ice were present during the early Cretaceous

222   2.4 Spin up Methodology

223   The oceans are the slowest evolving part of the modelled climate system and can take multiple

224   millennia to reach equilibrium, depending on the initial condition and climate state. In order to

225   speed up the convergence of the model, we initialized the ocean temperatures and salinity with the

226   values from previous model simulations from similar time periods. The atmosphere variables were

227   initialized in a similar manner. Although it is always possible that a different initialization procedure

228   may produce different final states, our experience is that the HadCM3 and HadCM3L have rarely

229   shown multiple equilibria.

230   The simulations were then run until they reached equilibrium, as defined by:

231   1. The globally and volume integrated annual mean ocean temperature trend is less than

232         $1^{\circ}C/1000$ year, in most cases considerably smaller than this.

233   2. The trends in surface air temperature are less than $0.3^{\circ}C/1000$ year

234   3. The net energy balance at the top of the atmosphere, averaged over 100-year period at the

235   end of the simulation, is less than 0.25 Wm^{-2} (in more than 80% of the simulations, the

236   imbalance is less than 0.1 Wm^{-2}). The Gregory plot (Gregory et al., 2004) implies surface

237   temperatures are within $0.3^{\circ}C$ of the equilibrium state.

238   These trends were chosen because they are less than typical orbital time scale variability (e.g.

239   temperature changes since the last deglaciation were approximately $5^{\circ}C$ over 10,000 years). Most

240   simulations were well within these criteria.   70% of simulations had residual net energy balances

241   less than 0.1 Wm^{-2}, but a few simulations were slower to reach full equilibrium. The resulting time

242   series of volume integrated global, annual mean ocean temperatures are shown in fig. 3.

243   The "smooth" CO_2 simulations were all run for 5000 model years and satisfied the criteria. The

244   Foster-CO_2 simulations were initially run for a minimum of 2000 years, at which point we reviewed

245   the simulations relative to the convergence criteria. If the simulations had not converged, we

246   extended the runs for an additional 3000 years. If they had not converged at the end of 5000 years,

247   we extended them again for an additional 3000 years. After 8000 years, all simulations had

248   converged based on the convergence criteria. In general, the slowest converging simulations

249   corresponded to some of the warmest climates (final temperatures in figure 3b and 3c were

250   generally warmer than in figure 3a) and almost all had significantly different final climates compared

251   to their initialization.

252

Results

3.1 Comparison of Deep Ocean Temperatures to Benthic Ocean Data

253

254

255 Before using the model to investigate the linkage of deep ocean temperatures to global mean

256 surface temperatures, it is interesting to evaluate whether the modelled deep ocean temperatures

257 agree with the deep ocean temperatures obtained from the isotopic studies of benthic foraminifera

258 (Friedrich et al., 2012; Zachos et al., 2008). It is important to note that the temperatures are likely to

259 be strongly influenced by the choice of CO_2, so we are not necessarily seeking perfect agreement but

260 to evaluate whether the model is within a plausible range. Figure 4a compares the modelled deep

261 ocean temperature to the foraminifera data from the Cenozoic and Cretaceous (115 Ma). The

262 observed isotope data are converted to temperature using the procedures described by (Hansen et

263 al., 2013).

264 The modelled deep temperature shown in fig.4a (solid line) is the average temperature at the

265 bottom level of the model, excluding depths less than 1000m. The observed data was collected from

266 a range of depths - including mid-ocean ridges whose depth can vary from 2000m to the true

267 bottom of the ocean. To evaluate whether this procedure gave a reasonable result, we also

268 calculated the global average temperature at the model layer depth closest to 2km (2116m). This is

269 shown by the dashed line in figure 4a. In general, the agreement between model bottom water

270 temperatures and 2km temperatures is very good. The standard deviation is 0.8˚C, and the

271 maximum difference is 1.6˚C. Compared to the overall variability, this is a relatively small difference.

272 The total change in benthic temperatures over the late Cretaceous and Cenozoic is well reproduced

273 by the model, with the "smooth" CO_2 record being particularly good. We do not expect the model to

274 represent sub-stage changes (100,000's of years) such as the PETM excursion or OAEs, but we do

275 expect that the broader temperature patterns should be simulated.

276 Comparison of the two simulations illustrates how strongly CO_2 controls global mean temperature.

277 The Foster-CO_2 driven simulation substantially differs from the estimates of deep-sea temperature

278 obtained from benthic forams and is generally a poorer fit to data. The greatest mismatch between

279 the Foster curve and the benthic temperature curve is during the late Cretaceous and early

280 Paleogene. Both dips in the Foster-CO_2 simulations correspond to relatively low estimates of CO_2

281 concentrations. This is because the dominant source of CO_2 values for these periods is from

282 paleosols (fig.1), which are often lower than other proxies. Unfortunately, the alternative CO_2

283 reconstructions of (Witkowski et al., 2018) have a data gap during this period.

284   A second big difference between the Foster curve and the benthic temperature curve occurs during

285   the Cenomanian-Turonian. This difference is similarly driven by a low estimate of CO_2 in the Foster-

286   CO_2 curve. These low CO_2 values are primarily based on stomatal density indices. Stomatal indices

287   also frequently suggest CO_2 levels lower than estimates obtained by other methods. The CO_2

288   estimates by (Witkowski et al., 2018) generally supports the higher levels of CO_2 (near to 1000

289   ppmv) that are suggested by the "smooth" CO_2 curve.

290   Both sets of simulations underestimate the warming during the middle Miocene. This issue has been

291   seen before in other models (You et al., 2009). In order to simulate the surface warmth of the middle

292   Miocene (15 Ma), CO_2 concentrations in the range 460–580 ppmv were required, whereas the CO_2

293   reconstructions for this period (Foster et al., 2017; Witkowski et al., 2018) are generally quite low

294   (250-400ppmv). This problem may be either due to the climate models having too low a climate

295   sensitivity or that the estimates of CO_2 are too low. It could also be related to a breakdown in the

296   relationship between temperatures and $\delta^{18}O$ of benthic forams.

297   The original compilation of (Zachos et al., 2008) represented a relatively small portion of the global

298   ocean and the implicit assumption was made that these results represented the entire ocean basin.

299   (Cramer et al., 2009) examined the data from an ocean basin perspective and suggested that these

300   inter-basin differences were generally small during the Late Cretaceous and early Paleogene (90Ma –

301   35 Ma) and the differences between ocean basins were larger during the late Paleogene and early

302   Neogene. Our model largely also reproduces this pattern. Figure 5 shows the ocean temperature at

303   2116 m during the late Cretaceous (69 Ma), the late Eocene (39 Ma) and the Oligocene (31 Ma) for

304   the "smooth"-CO_2 simulations. In the late Cretaceous, the model temperatures are almost identical

305   in the North Atlantic and Pacific (8˚C – 10˚C). There is warmer deep water forming in the Indian

306   Ocean (deep mixed layer depths, not shown), off the West coast of Australia (10˚C – 12˚C), but

307   otherwise the pattern is very homogeneous. This is in agreement with some paleo reconstructions

308   for the Cretaceous (e.g. (Murphy and Thomas, 2012).

309   By the time we reach the late Eocene (39 Ma), the North Atlantic and Pacific remain very similar but

310   cooler deep water (6˚C – 8˚C) is now originating in the South Atlantic. The South Atlantic cool

311   bottom water source remains in the Oligocene, but we see a strong transition in the North Atlantic

312   to an essentially modern circulation with the major source of deep, cold water occurring in the high

313   southerly latitudes (3˚C – 5˚C) and strong gradient between the North Atlantic and Pacific.

314   3.2 Comparison of Model Sea Surface Temperature to Proxy Data

315   The previous section focused on benthic temperatures, but it is also important to evaluate whether

316   the modelled sea surface temperatures are plausible (within the uncertainties of the CO_2

317   reconstructions). Figure 4b shows a comparison between the model simulations of sea surface

318   temperature and two published synthesis of proxy SST data. (O'Brien et al., 2017) compiled TEX_{86}

319   and $\delta^{18}O$ for the Cretaceous, separated into tropical and high-latitude (polewards of 48°) regions.

320   (Cramwinckel et al., 2018) compiled early Cenozoic tropical SST data, using Tex_{86}, $\delta^{18}O$, Mg/Ca and

321   clumped isotopes. We compare these to modelled SST for the region 15°S to 15°N, and for the

322   average of Northern and Southern hemispheres between 47.5° and 60°. The proxy data includes

323   sites from all ocean basins and so we also examined the spatial variability within the model. This

324   spatial variability consists of changes along longitude (effectively different ocean basins) and

325   changes with latitude (related to the gradient between equator and pole). We therefore calculated

326   the average standard deviation of SST relative to the zonal mean at each latitude (this is shown by

327   the smaller tick marks) and the total standard deviation of SST relative to the regional average. In

328   practice, the equatorial values are dominated by inter-basin variations and hence the two measures

329   of spatial variability are almost identical. The high latitude variability has a bigger difference

330   between the longitudinal variations and the total variability, because the equator-to-pole

331   temperature gradient (i.e. the temperatures at the latitude limits of the region are a few degrees

332   warmer/colder than the average). The spatial variability was very similar for the "smooth"-CO_2 and

333   Foster-CO_2 simulations so, for clarity, on figure 4b we only show the results as error bars on the

334   model Foster-CO_2 simulations.

335   Overall, the comparison between model and data is generally reasonable. The modelled equatorial

336   temperatures largely follow the data, albeit with considerable scatter in the data. Both simulations

337   tend to be towards the warmest equatorial data in the early Cretaceous (Albian). These

338   temperatures largely come from Tex_{86} data. There are many $\delta^{18}O$ based SST which are significantly

339   colder during this period. This data almost exclusively comes from cores 1050/1052 which are in the

340   Gulf of Mexico. It is possible that these data are offset due to a bias in the $\delta^{18}O$ of sea water because

341   of the relatively enclosed region. The Foster-CO_2 simulations are noticeably colder than the data at

342   the Cenomanian peak warmth, which is presumably related to the relatively low CO_2 as discussed for

343   the benthic temperatures. The benthic record also showed a cool (low CO_2) bias in the late

344   Cretaceous. This is not such an obvious feature of the surface temperatures. The Foster simulations

345   are colder than the "smooth"-CO_2 simulations during the late Cretaceous but there is not a strong

346   mismatch between model and data. Both simulations are close to the observations, though the

347   "smooth"-CO_2 simulations better matches the high-latitude data (but is slightly poorer with the

348   tropical data).

349   The biggest area of disagreement between mode and data is at the high latitudes in the mid-

350   Cretaceous warm period. As expected, the model is considerably cooler than the data, with a 10-

351 15°C mismatch between models and data. If we assume that the data has a seasonal bias, and select

352 the summer seasons from the model, then the mismatch is slightly reduced by about 4°C. The

353 problem of a cool high latitudes in models is seen in many model studies and there is increasing

354 evidence that this is related to the way that the models simulate clouds ((Kiehl and Shields, 2013);

355 (Sagoo et al., 2013); (Zhu et al., 2019)).

Correlation of Deep Ocean Temperatures to Polar Sea Surface Temperatures

357 The previous sections showed that that the climate model was producing a plausible reconstruction

358 of past ocean temperature changes, at least within the uncertainties of the CO_2 estimates. We now

359 use the HadCM3L model to investigate the links between deep ocean temperature and global mean

360 surface temperature.

361 In theory, the deep ocean temperature should be correlated with the sea surface temperature at the

362 location of deep-water formation which is normally assumed to be high latitude surface waters in

363 winter. We therefore compare deep ocean temperatures (defined as the average temperature at the

364 bottom of the model ocean, where the bottom must be deeper than 1000 m) with the average

365 winter sea surface temperature polewards of 60° (fig. 6). Winter is defined as December, January,

366 and February in the northern hemisphere and June, July, and August in the southern hemisphere.

367 Also shown in Figure 6 is the best fit line, which has a slope of 0.40 (+/-0.05 at the 97.5% level), an r^2

368 of 0.59, and a standard error of 1.2°C. We obtained very similar results when we compared the polar

369 sea surface temperatures with the average temperature at 2116m instead of the true benthic

370 temperatures. We also compared the deep ocean temperatures to the mean polar sea surface

371 temperatures when the mixed layer depth exceeded 250 m (poleward of 50°). The results were

372 similar although the scatter was somewhat larger (r^2=0.48).

373 Overall, the relationship between deep ocean temperatures and polar sea surface temperatures is

374 clear (Figure 6) but there is considerable scatter around the best fit line, especially at the high end,

375 and the slope is less steep than perhaps would be expected (Hansen and Sato, 2012). The scatter is

376 less for the Cenozoic and late Cretaceous (up to 100 Ma; green and orange dots and triangles). If we

377 used only Cenozoic and late Cretaceous simulations, then the slope is similar (0.43) but r^2=0.92 and

378 standard error=0.47°C. This provides strong confirmation that benthic data is a robust

379 approximation to polar surface temperatures when the continental configuration is similar to the

380 present.

381 However, the scatter is greater for older time periods, with the largest divergence observed for the

382 warm periods of the Triassic and early Jurassic, particularly for the Foster CO_2 simulations (purple

383 and blue dots). Examination of climate models for these time periods reveals relatively sluggish and

384   shallow ocean circulation. For instance, in the Ladinian stage, mid-Triassic (~240Ma) the overturning

385   circulation is extremely weak (Fig. 7). The maximum strength of the northern hemisphere

386   overturning cell is less than 10 Sv and the southern cell is less than 5 Sv. Under these conditions,

387   deep ocean water does not always form at polar latitudes. Examination of the mixed layer depth

388   (not shown) shows that during these time periods, the deepest mixed layer depths are in the sub-

389   tropics. In subtropics, there is very high evaporation relative to precipitation (due to the low

390   precipitation and high temperature. This produces highly saline waters that sink and spread out into

391   the global ocean. This mechanism has been previously suggested as a mechanism for warm

392   Cretaceous deep water formation (Brass et al., 1982), (Kennett and Stott, 1991). This mechanism for

393   warm deep water formation has also been seen in other climate models (e.g. (Poulsen et al., 2001)).

394   Though it is not a pre-requisite for warm deep-water formation and is thus, potentially, a model-

395   dependent result.

396   The correlation between deep ocean temperatures and the temperature of polar surface waters

397   differs between the "smooth" CO_2 simulations and the Foster CO_2 simulations. The slope is only 0.30

398   (r^2=0.57) for the "smooth" CO_2 simulations whereas the slope is 0.48 (r^2=0.65) for the Foster

399   simulations. This is because CO_2 is a strong forcing agent that influences both the surface and deep

400   ocean temperatures. By contrast, if the CO_2 does not vary as much, then the temperature does not

401   vary as much, and the influence of paleogeography becomes more important. These

402   paleogeographic changes generally cause subtle and complicated changes in ocean circulation that

403   affect the location and latitude of deep-water formation.

404   In contrast, the mid-Cretaceous is also very warm but the continental configuration (specifically, land

405   at high southern latitudes) favors the formation of cool, high latitude deep water. Throughout the

406   Cretaceous there is significant southern high latitude source of deep water and hence deep-water

407   temperatures are well correlated with surface high latitude temperatures. The strength of this

408   connection, however, may be over exaggerated in the model. Like many climate models, HadCM3

409   underestimates the reduction in the pole-to-Equator sea surface temperature. This means that

410   during the Cretaceous the high latitudes are probably too cold. Consequently, some seasonal sea ice

411   does form which encourages the formation of cold deep-water, via brine rejection.

412   In the late Eocene (~40 Ma), the ocean circulation is similar to the Cretaceous, but the strong

413   southern overturning cell is closer to the South Pole, indicating that the main source of deep water

414   has moved further polewards. The poleward movement of the region of downwelling waters

415   explains some of the variability between deep ocean temperatures and temperature of polar surface

416   waters.

417   For reference, we also include the present-day meridional circulation. The modern southern

418   hemisphere circulation is essentially a strengthening of late Eocene meridional circulation. The

419   Northern hemisphere is dominated by the Atlantic meridional overturning circulation. The Atlantic

420   circulation pattern does not resemble the modern pattern of circulation until the Miocene.

Surface Polar Amplification

422   The conceptual model used to connect benthic ocean temperatures to global mean surface

423   temperatures assumes that there is a constant relationship between high latitude sea surface

424   temperatures and global mean annual mean surface air temperature. (Hansen and Sato, 2012)

425   argue that this amplification is partly related to ice-albedo feedback but also includes a factor

426   related to the contrasting amplification of temperatures on land compared to the ocean. To

427   investigate the stability of this relationship, fig. 8 shows the correlation between polar winter sea

428   surface temperatures (60° - 90°) and global mean surface air temperature. The polar temperatures

429   are the average of the two winter hemispheres (i.e. average of DJF polar SSTs in the Northern

430   hemisphere and JJA polar SSTs in the Southern hemisphere). Also shown is a simple linear

431   regression, with an average slope of 1.3 and with an r^2 = 0.79. If we only use Northern polar winter

432   temperatures, the slope is 1.1; if we only use Southern polar winter temperatures, then the slope is

433   0.7. Taken separately, the scatter about the mean is considerably larger (r^2 of 0.5 and 0.6

434   respectively) than the scatter if both data sets are combined (r^2 = 0.79).

435   As expected, there appears to be a strong non-linear component to the correlation. There are two

436   separate regimes: 1) one with a steeper slope during colder periods (average polar winter

437   temperature less than about 1^oC), and 2) a shallower slope for warmer conditions. This is strongly

438   linked to the extent of sea-ice cover. Cooler periods promote the growth of sea-ice which

439   strengthens the ice-albedo feedback mechanism resulting in a steeper temperature gradient (strong

440   polar amplification). Conversely, the warmer conditions result in less sea ice and hence a weaker sea

441   ice-albedo feedback resulting in a weaker temperature gradient (reduced polar amplification).

442   Examining the Foster CO_2 and "smooth" CO_2 simulations reveals an additional factor. If we examine

443   the "smooth" CO_2 simulations only, then the best fit linear slope is slightly less than the average

444   slope (1.1 vs 1.3). This can be explained by the fact that we have fewer very cold climates

445   (particularly in the Carboniferous) due to the relatively elevated levels of CO_2. However, the scatter

446   in the "smooth" CO2 correlation is much larger, with an r^2 of only 0.66. By comparison, correlation

447   between Global Mean Surface Temperature and Polar Sea Surface Temperature using the Foster CO_2

448   has a similar overall slope to the combined set and a smaller amount of scatter. This suggests that

449   CO2 forcing and polar amplitude forcing have an important impact on the relationship between

450   global and polar temperatures. The variations of carbon dioxide in the Foster set of simulations are

451   large and they drive large changes in global mean temperature. Conversely significant sea-ice albedo

452   feedbacks characterize times when the polar amplification is important. There are several well

453   studied processes that lead to such changes, including albedo effects from changing ice but also

454   from poleward heat transport changes, cloud cover, and latent heat effects ((Alexeev et al., 2005;

455   Holland and Bitz, 2003; Sutton et al., 2007)). By contrast, the "smooth" CO_2 simulations have

456   considerably less forcing due to CO_2 variability which leads to a larger paleogeographic effect. For

457   instance, when there is more land at the poles, there will be more evaporation over the land areas

458   and hence simple surface energy balance arguments would suggest different temperatures ((Sutton

459   et al., 2007)) .

460   In figure 8, there are a few data points which are complete outliers. These correspond to simulations

461   in the Ordovician; the outliers happen irrespective of the CO_2 model that is used. Inspection of these

462   simulations shows that the cause for this discrepancy is related to two factors: 1) a continental

463   configuration with almost no land in the Northern hemisphere and , 2) a reconstruction which

464   includes significant southern hemisphere ice cover (see fig.1 and fig 2). Combined, these factors

465   produced a temperature structure which is highly non-symmetric, with the Southern high latitudes

466   being more than 20°C colder than the Northern high latitudes. This anomaly biases the average polar

467   temperatures shown in figure 8.

468   Deep Ocean Temperature versus Global Mean Temperature

469   The relationships described above help to understand the overall relationship between deep ocean

470   temperatures and global mean temperature. Figure 9 shows the correlation between modelled deep

471   ocean temperatures (> 1000 m) and global mean surface air temperature, and figure 10 shows a

472   comparison of changes in modelled deep ocean temperature compared to model global mean

473   temperature throughout the Phanerozoic.

474   The overall slope is 0.64 (0.59 to 0.69) with an r^2 = 0.74. If we consider the last 115 Ma (for which

475   exists compiled benthic temperatures), then the slope is slightly steeper (0.67 with an r^2 = 0.90).

476   Similarly, the "smooth"-CO_2 and the Foster-CO_2 simulation results have very different slopes. The

477   "smooth"-CO_2 simulations have a slope of 0.47, whereas the Foster-CO_2 simulations have a slope of

478   0.76. The root mean square departure from the regression line in figure 9 is 1.3°C.

479   The relatively good correlations in the fig.9 are confirmed when examining fig.10a and 10b. On

480   average, the deep ocean temperatures tend to underestimate the global mean change (fig.10b)

481   which is consistent with the regression slope being less than 1. However, the errors are substantial

482   with largest errors occurring during the pre-Cretaceous and can be 4-6 °C. This is an appreciable

483   error that would have a substantial impact on estimates of climate sensitivity. Even within the late

484   Cretaceous and Cenozoic, the errors can exceed 2°C which can exceed 40% of the total change.

485   The characteristics of the plots can best be understood in terms of figures (6 and 8). For instance,

486   most of the Carboniferous simulations plot below the regression line because the polar SSTs are not

487   well-correlated with the global mean temperature (figure 8). By contrast, the Triassic and Jurassic

488   Foster CO_2 simulations plot above the regression line because the deep ocean temperature is not

489   well-correlated with the polar temperatures (figure 6).

490   ## Discussion and Conclusion

491   The paper has presented the results from two unique sets of paleoclimate simulations covering the

492   Phanerozoic. The focus of the paper has been to use the HadCM3L climate model to evaluate how

493   well we can predict global mean surface temperatures from benthic foram data. This is an important

494   consideration because benthic microfossil data are one of the few datasets used to directly estimate

495   past global mean temperatures. Other methods, such as using planktonic foraminiferal estimates,

496   are more challenging because the sample sites are geographically sparse, so it is difficult to

497   accurately estimate the global mean temperature from highly variable and widely dispersed data.

498   This is particularly an issue for older time periods when fewer isotopic measurements from

499   planktonic microfossils are available, and can result in a bias because most of the isotopic

500   temperature sample localities are from tropical latitudes (30˚S − 30˚N) (Song et al., 2019).

501   By contrast, deep ocean temperatures are more spatially uniform. Hence. benthic foram data has

502   frequently been used to estimate past global mean temperatures and climate sensitivity (Hansen et

503   al., 2013). Estimates of uncertainty for deep ocean temperatures incorporate uncertainties from CO_2

504   and from the conversion of $\delta^{18}O$ measurements to temperature but have not been able to assess

505   assumptions about the source regions for deep ocean waters and the importance polar

506   amplification. Of course, in practice, lack of ocean sea floor means that benthic compilations exist

507   only for the last 110Ma.

508   We have shown that although the expected correlation between benthic temperatures and high-

509   latitude surface temperatures exists, the correlation has considerable scatter. This is caused by

510   several factors. Changing paleogeographies results in changing locations for deep water formation.

511   Some paleogeographies result in significant deep-water formation in the Northern hemisphere (e.g.

512   our present-day configuration) although for most of the Phanerozoic, the dominant source of deep-

513   water formation has been southern hemisphere. Similarly, even when deep water is formed in just

514   one hemisphere, there can be substantial regional and latitudinal variations in its location and the

515   corresponding temperatures. Finally, during times of very warm climates (e.g. mid-Cretaceous) the

516   overturning circulation can be very weak and there is a marked decoupling between the surface

517   waters and deep ocean. In the HadCM3 model during hothouse time periods, high temperatures and

518   high rates of evaporation produce hot and saline surface waters which sink to become intermediate

519   and deep waters at low latitudes.

520   Similar arguments can be made regarding the link between global mean temperature and the

521   temperature at high latitudes. Particularly important is the area of land at the poles and the extent

522   of sea ice/land ice. Colder climates and paleogeographic configurations with more land at the pole

523   will result in a steeper latitudinal temperature gradient and hence exhibit a changing relationship

524   between polar and global temperatures. But the fraction of land versus ocean is also important.

525   Finally, the overall relationship between deep ocean temperatures and global mean temperature is

526   shown to be relatively linear, but the slope is quite variable. In the model simulations using the

527   "smooth" CO_2 curve, the slope is substantially shallower (0.48) than slope obtained using the Foster

528   CO_2 curve (0.76). This is related to the different controls that CO_2 and paleogeography exert (as

529   discussed above). In the simulation that uses the "smooth" CO_2 data set, the levels of CO_2 do not

530   vary much, so the paleogeographic controls are more pronounced.

531   This raises the interesting conundrum that when trying to use reconstructed deep ocean

532   temperatures and CO_2 to estimate climate sensitivity, the interpreted global mean temperature also

533   depends, in part, on the CO_2 concentrations. However, if we simply use the combined slope, then

534   the root mean square error is approximately 1.4˚C, and the maximum error is over 4ºC. The root

535   mean square error is a relatively small compared to the overall changes and hence the resulting

536   uncertainty in climate sensitivity associated with this error is relatively small (~15%) and the CO_2

537   uncertainty dominates. However, the maximum error is potentially more significant.

538   Our work has not addressed other sources of uncertainty. In particular, it would be valuable to use a

539   water isotope-enabled climate model to better address the uncertainties associated with the

540   conversion of the observed benthic $\delta^{18}O$ to temperature. This requires assumptions about the $\delta^{18}O$

541   of sea water. We hope to perform such simulation in future work, though this is a particularly

542   challenging computational problem because the isotope enabled model is significantly slower and

543   the completion of the multi-millennial simulations required for deep ocean estimates would take

544   more than 18 months to complete.

545   Our simulations extend and develop those published by (Lunt et al., 2016), and (Farnsworth et al.,

546   2019a; Farnsworth et al., 2019b). The simulations reported in this paper used the same climate

547   model (HadCM3L) but used an improved ozone concentration and corrected a salinity drift that can

548   lead to substantial changes over the duration of the simulation. Our simulations also use an

549 alternative set of geographic reconstructions that cover a larger time period (540 Ma – Modern).

550 They also include realistic land ice cover estimates, which were not included in the original

551 simulations (except for the late Cenozoic) but generally have a small impact in the Mesozoic.

552 Similarly, the new simulations use two alternative models for past atmospheric CO_2 use more

553 realistic variations in CO_2 through time, while at the same time recognizing the levels of uncertainty.

554 Although the Foster CO_2 curve is more directly constrained by CO_2 data, it should be noted that this

555 data come from multiple proxies and there are large gaps in the data set. There is evidence that the

556 different proxies have different biases and it is not obvious that the correct approach is to simply fit

557 a Loess-type curve to the CO_2 data. This is exemplified by the Maastrichtian. The Foster Loess curve

558 shows a minimum in CO_2 during the Maastrichtian which results in the modelled deep ocean

559 temperatures being much too cold. However, detailed examination of the CO_2 data shows most of

560 the Maastrichtian data is based on stomatal index reconstructions which often are lower than other

561 proxies. Thus, the Maastrichtian low CO_2, relative to other periods, is potentially driven by changing

562 the proxy rather than by real temporal changes.

563 Though the alternative, "smooth" CO_2 curve is not the optimum fit to the data, it does pass through

564 the cloud of individual CO_2 reconstructions and hence represents one possible "reality". For the Late

565 Cretaceous and Cenozoic, the "smooth" CO_2 simulation set does a significantly better job simulating

566 the deep ocean temperatures of the Friedrich/Cramer/Zachos curve.

567 Although the focus of the paper has been the evaluation of the modelled relationship between

568 benthic and surface temperatures, the simulations are a potentially valuable resource for future

569 studies. This includes using the simulations for paleoclimate/climate dynamic studies and for climate

570 impact studies, such as ecological niche modelling. We have therefore made available on our

571 website the results from our simulations

572 (https://www.paleo.bristol.ac.uk/ummodel/scripts/papers/Valdes_et_al_2021.html)

573 Data Availability

574 All simulation data is available from:
575 https://www.paleo.bristol.ac.uk/ummodel/scripts/papers/Valdes_et_al_2021.html

576 Author contributions
577 Study was developed by all authors. All model simulations were performed by PJV who also
578 prepared the manuscript with contributions from all co-authors.

579 Competing interests

580 The authors declare that they have no conflict of interest

581

582

Acknowledgments.

584 DJL and PJV acknowledge funding from NERC through NE/P013805/1. The production of

585 paleogeographic digital elevation models was funded by the sponsors of the PALEOMAP Project.

586 This work is part of the PhanTASTIC project led by Scott Wing and Brian Huber from the Smithsonian

587 Institution's National Museum of Natural History and was initiated at a workshop supported by

588 Roland and Debra Sauermann. This work was carried out using the computational facilities of the

589 Advanced Computing Research Centre, University of Bristol (http://www.bris.ac.uk/acrc/). The

590 authors declare that they have no competing interests. Data and materials availability: All data

591 needed to evaluate the conclusions in the paper are present in the paper. Model data can be

592 accessed at www.bridge.bris.ac.uk/resources/simulations.

593

594

595

596

597

598

599 Figures

600 Figure 1. Summary of boundary condition changes to model of the Phanerozoic, (a) CO_2

601 reconstructions (from Foster et al. 2017) and the two scenarios used in the models, (b) Land-sea

602 fraction from the paleogeographic reconstructions, and (c) land ice area input into model. The

603 paleogeographic reconstructions can be accessed at https://www.earthbyte.org/paleodem-

604 resource-scotese-and-wright-2018/. An animation of the high-resolution (1° x 1°) and model

605 resolution (3.75° longitude x 2.5° latitude) maps can be found here:

606 https://www.paleo.bristol.ac.uk/~ggpjv/scotese/scotese_raw_moll.normal_scotese_moll.normal.ht

607 ml
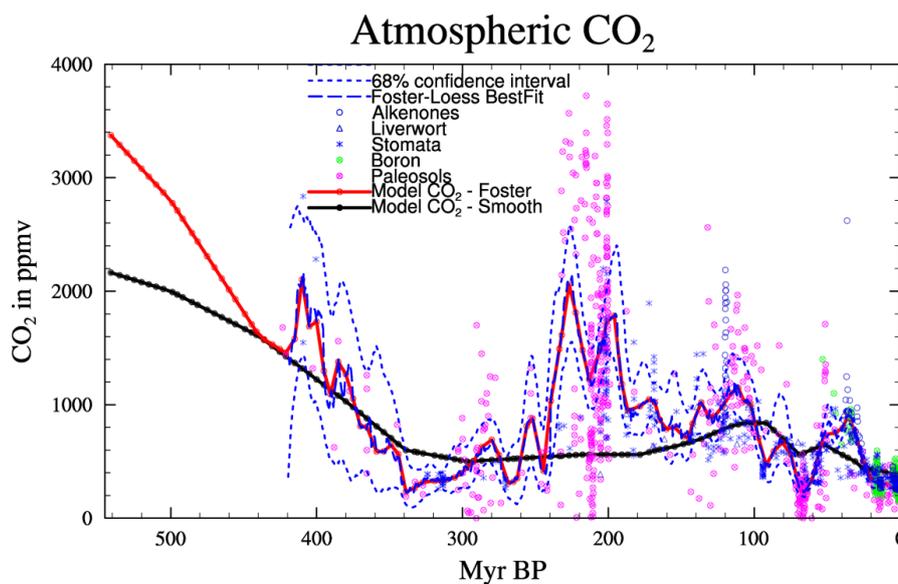
608
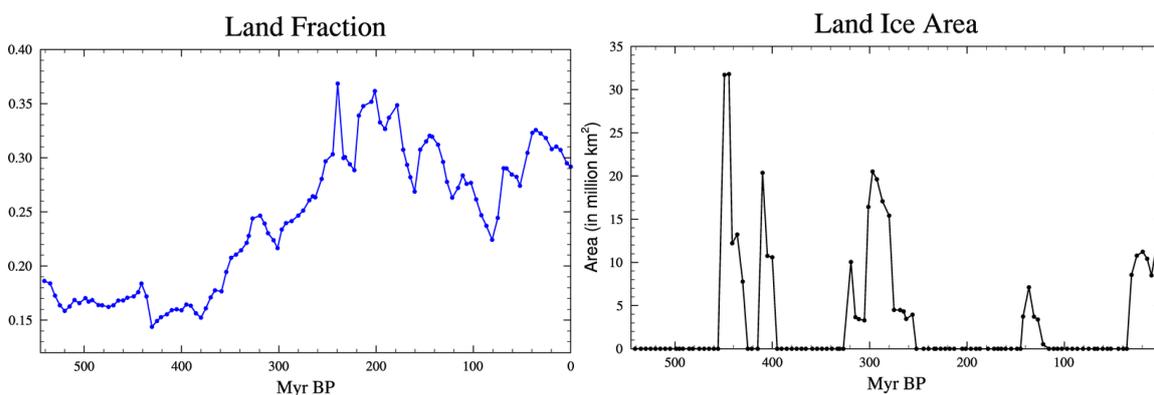
609

610

611 Figure 2. A few example paleogeographies, once they have been re-gridded onto the HadCM3L grid.

612 The examples are for (a) present day, (b) Albian, 102.6Ma (Lower Cretaceous), (c) Hettangian,

613 201.3Ma (lower Jurassic), (d) Moscovian, 311.1Ma (Pennsylvanian, Carboniferous), (e) Katian,

614 449.1Ma (Upper Ordovician), and (f) Fortunian, 541.0Ma (Cambrian). The top color legend refers to

615 the height of the ice sheets (if they exist), the middle color legend refers to heights on land (except

616 ice), and the lower color legend refers to the ocean bathymetry. All units are meters.

617

618

619
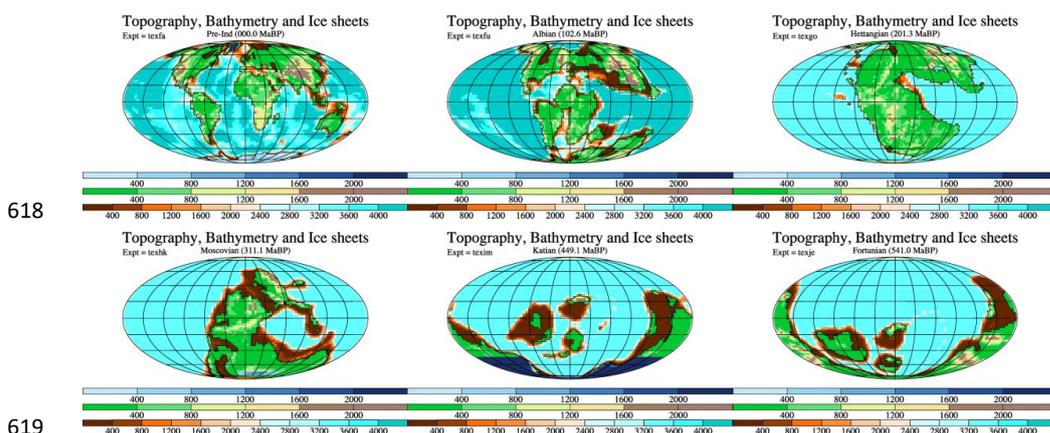
620

621

622

623

624

625

626

627

628

629   Figure 3. Time series of the annual, volume mean ocean temperature for all 109 simulations. (a)

630   shows those simulations for which 2000 years was sufficient to satisfy the convergence criteria

631   described in text (these were for all simulations listed in table 1 except those listed in (b) and (c)), (b)

632   those simulation which required 5000 years (these were for all the simulations for 31.0, 35.9, 39.5,

633   55.8, 60.6, 66.0, 69.0, 102.6, 107.0, 121.8, 127.2, 154.7, 160.4, 168.2, 172.2, 178.4, 186.8, 190.8,

634   196.0, 201.3, 204.9, 213.2, 217.8, 222.4, 227.0, 232.0, and 233.6 Ma BP), and (c) those simulation

635   which required 8000 years (these were simulations for 44.5, 52.2, 86.7, 91.9, 97.2, 111.0, 115.8,

636   131.2, 136.4, 142.4, 145.0, 148.6, 164.8, and 239.5 Ma BP)

637
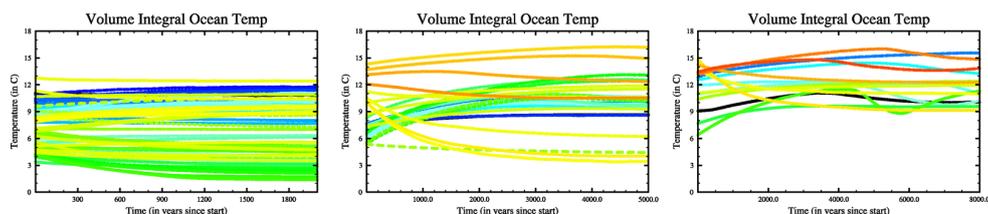
638

639

640

641   Figure 4. (a) Comparison of modelled deep ocean temperatures versus those from (Zachos et al.,

642   2008) and (Friedrich et al., 2012) converted to temperature using the formulation in (Hansen et al.,

643   2013). The model temperatures are global averages over the bottom layer of the model but excludes

644   shallow marine settings (less than 300m). The dashed lines show the modelled global average ocean

645   temperatures at the model layer centered at 2116m, and (b) Comparison of modelled sea surface

646   temperatures with the compilations of (O'Brien et al., 2017) and (Cramwinckel et al., 2018). The data

647   is a combination of Tex$_{86}$ (using the TexH calibration), $\delta^{18}O$ (using Bemis et al. calibration, with a

648   correction for the latitudinal gradient of $\delta^{18}O$) Mg/Ca, and clumped Isotope data (from (Evans et al.,

649   2018)). The model data shows low latitude temperatures (averaged from 10S to 10N) and high

650   latitude temperatures (averaged over 47.5N to 65N and 47.5S to 65S). The Foster-CO$_2$ simulations

651   also show a measure of the spatial variability. The large bars show the spatial standard deviation

652   across the whole region, and the smaller bars shows the average spatial standard deviation along

653   longitudes within the region. Note that the ranges of both the x and y-axis differ between (a) and (b).
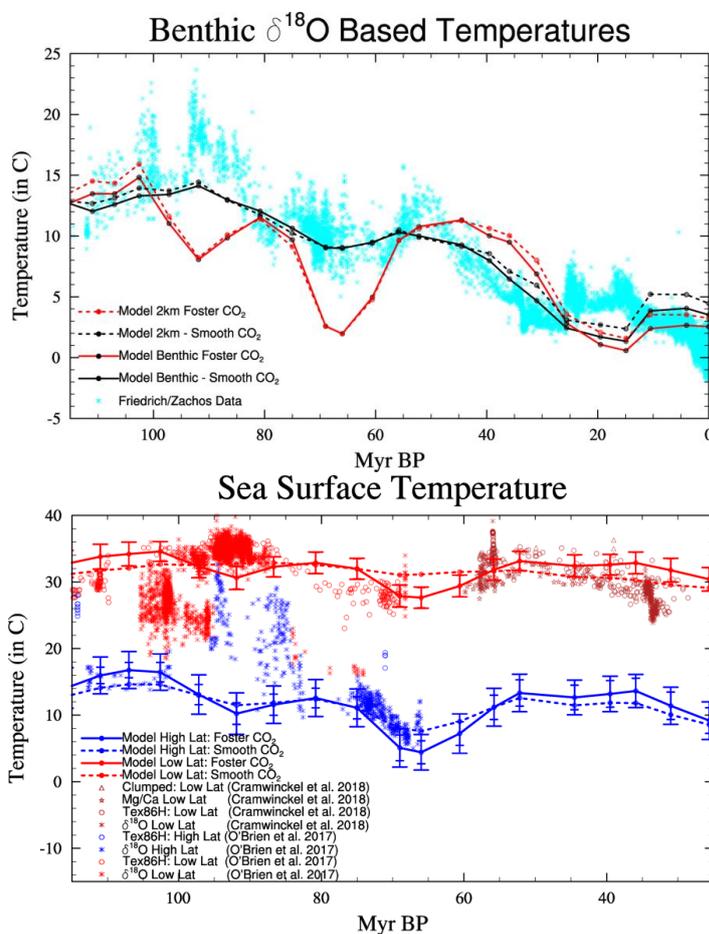
654   Figure 5. Modelled annual mean ocean temperatures are 2116m depth for three example past time

655   periods. The left figure is for the late Cretaceous, the center for the late Eocene (39.5Ma), and the

656   right for the Oligocene (31Ma). These are results from the smooth-CO_2 set of simulations which

657   agree better with the observed benthic temperature data. Also included are the pre-industrial

658   simulation and World Ocean Atlas 1994 observational data, provided by the NOAA-ESRL Physical

659   Sciences Laboratory, Boulder Colorado from their web site at https://psl.noaa.gov/. The thin black

660   lines show the coastlines and the grey areas are showing where the ocean is shallower than 2116m.

661

662
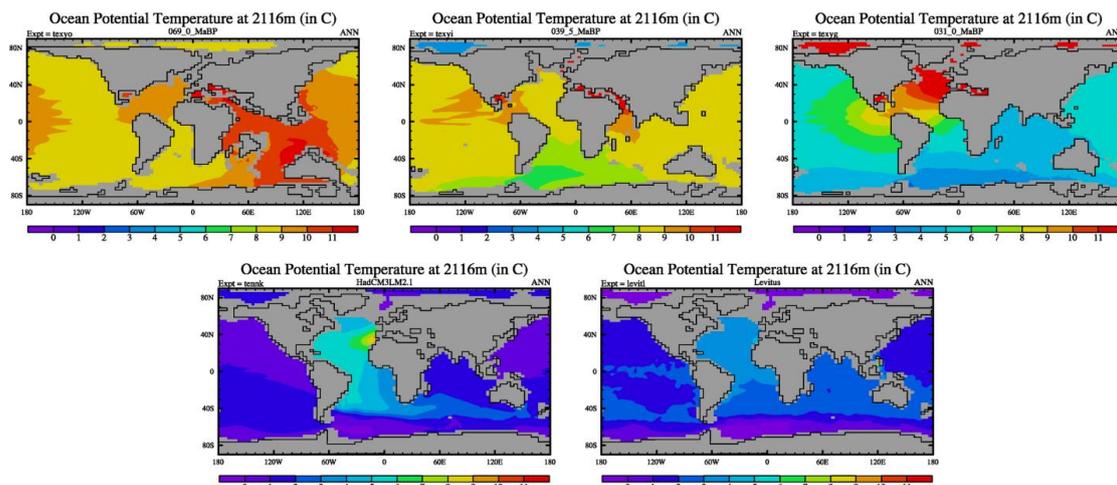
Figure 6. Correlations between deep ocean temperatures and surface polar sea surface temperatures. The deep ocean temperatures are defined as the average temperature at the bottom of the model ocean, where the bottom must be deeper than 1000m. The polar sea surface temperatures are the average winter (i.e. northern polar in DJF and southern polar in JJA) sea surface temperature polewards of 60°. The inverted triangles show the results from the smooth CO_2 simulations and the dots refer to the Foster CO_2 simulations. The colors refer to different geological era.
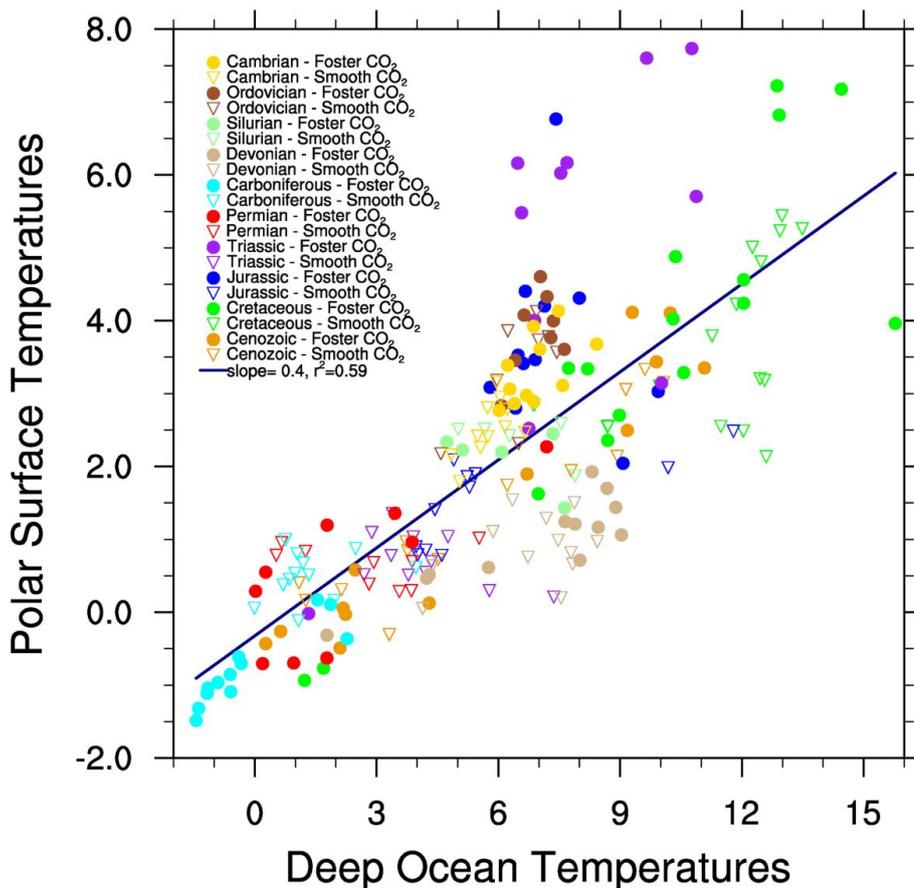
671 Figure 7. Global Ocean overturning circulation (in Sverdrup) for four different time periods for the

672 Foster-CO$_2$ simulations. Positive (yellow/red) values correspond to a clockwise circulation, negative

673 (dark blue/purple) values represent an anti-clockwise circulation. Top left: Middle Triassic, Ladinian,

674 239.5Ma, top right: Lower Cretaceous, Aptian, 121.8 Ma, bottom left: Late Eocene, Bartonian,

675 39.5Ma, and bottom right: Present Day.

676
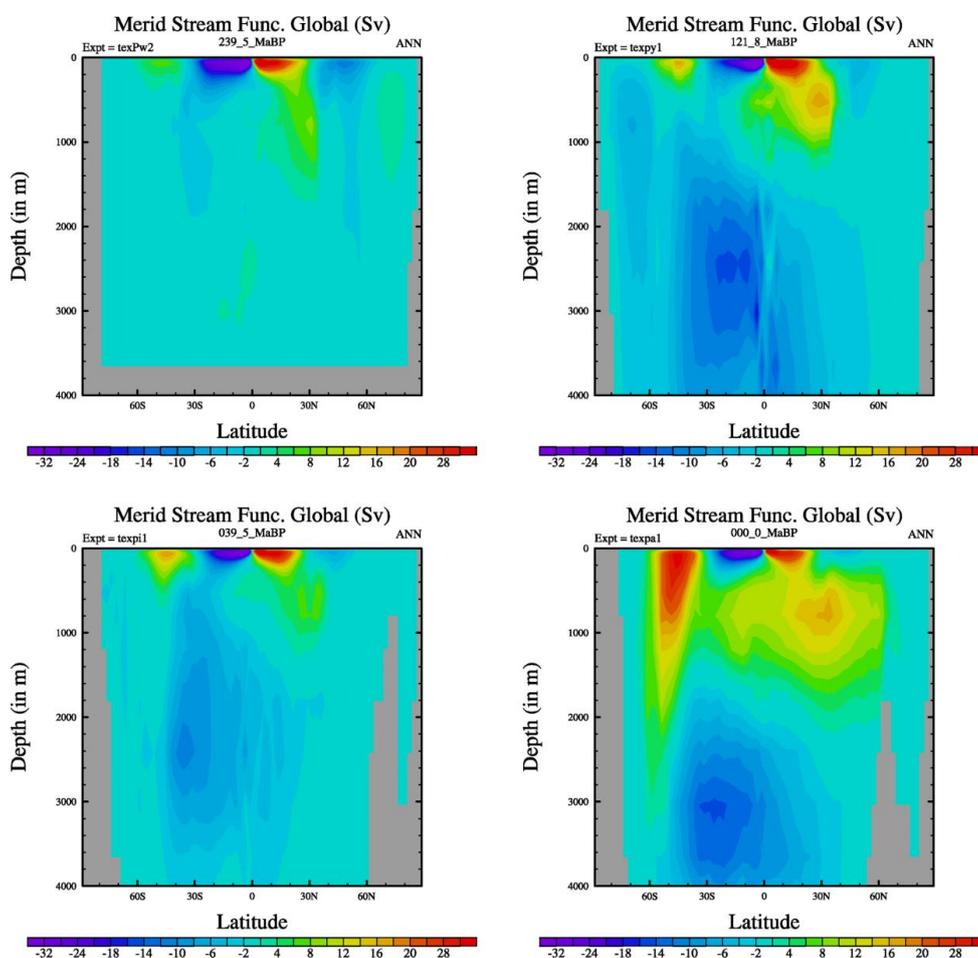
677

678

679 **Figure 8**. Correlation between high latitude ocean temperatures (polewards of 60°) and the annual

680 mean, global mean surface air temperature. The polar temperatures are the average of the two

681 winter hemispheres (i.e. northern DJF and southern JJA). Other details as in figure 6.

682

683
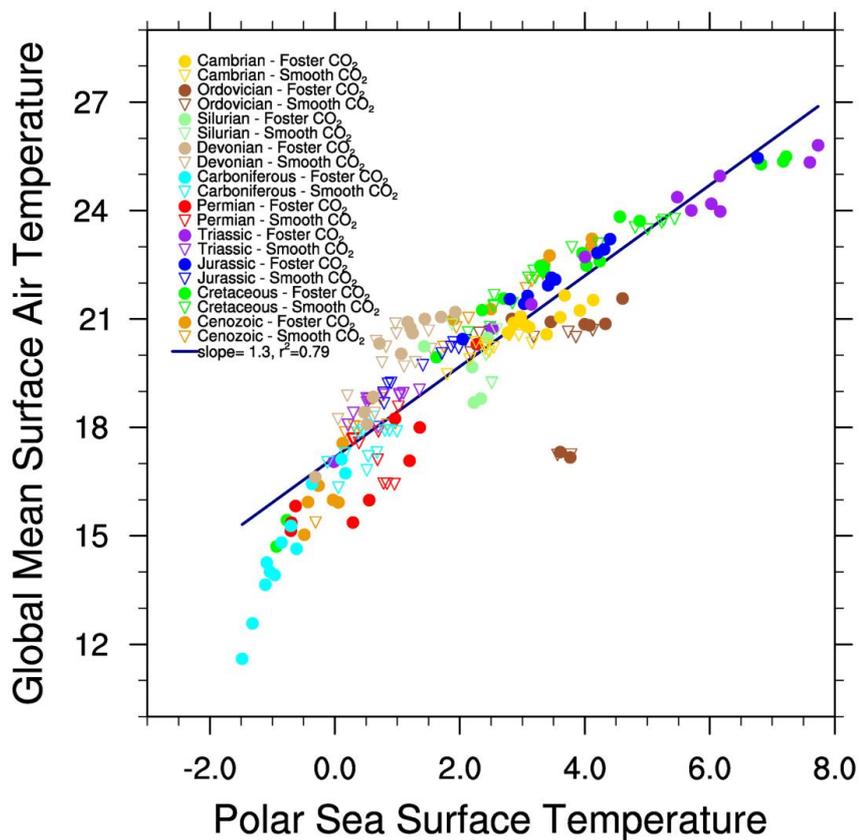
684

685   Figure 9. Correlation between the global mean, annual mean surface air temperature and the deep

686   ocean temperature. The deep ocean temperatures are defined as the average temperature at the

687   bottom of the model ocean, where the bottom must be deeper than 1000m. Other details as in

688   figure 6.

689
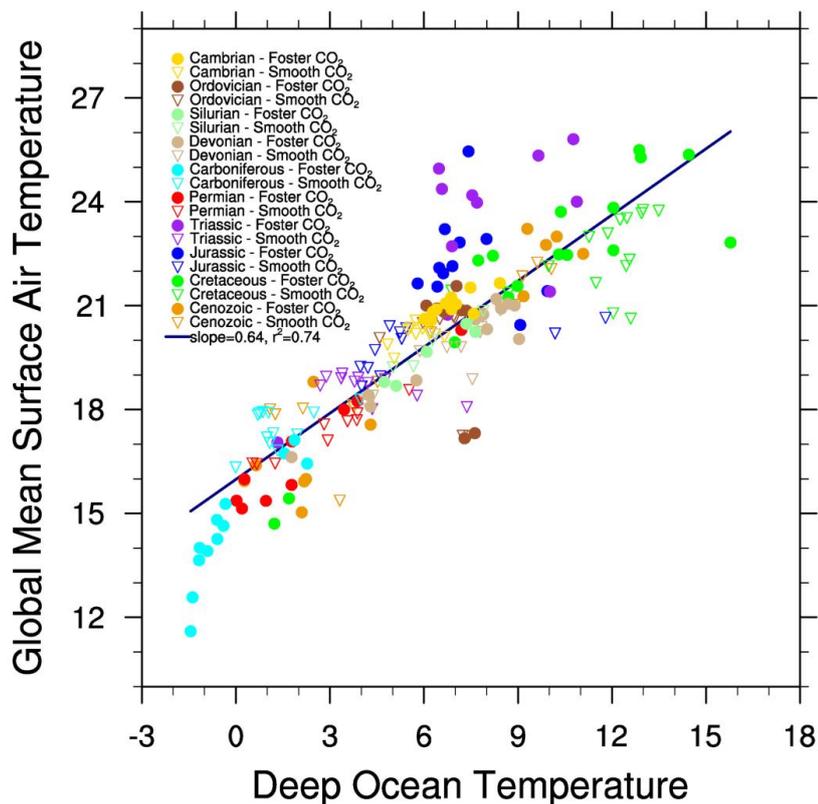
690

691

692   Figure 10. Phanerozoic Time series of modelled temperature change (relative to pre-Industrial) for

693   the smooth (green lines) and Foster-CO_2 (black) simulations (a) shows the actual modelled global

694   mean surface air temperature (solid lines) whereas the dashed line shows the estimate based on

695   deep ocean temperatures, and (b) error in the estimate of global mean temperature change if based

696   on deep ocean temperatures (i.e. deep ocean – global mean surface temperatures).

697

Climate of the Past

Discussions
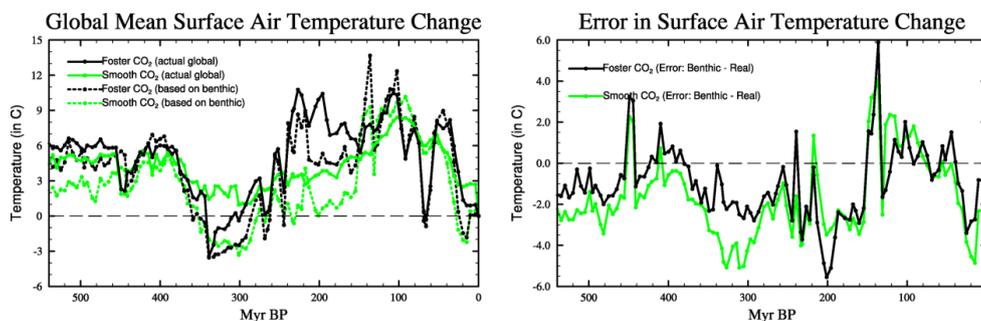
References

698 References

699 Alexeev, V.A., Langen, P.L., Bates, J.R., 2005. Polar amplification of surface warming on an
700 aquaplanet in "ghost forcing" experiments without sea ice feedbacks. Clim. Dyn. 24, 655-666.
701 Baatsen, M., van Hinsbergen, D.J.J., von der Heydt, A.S., Dijkstra, H.A., Sluijs, A., Abels, H.A., Bijl, P.K.,
702 2016. Reconstructing geographical boundary conditions for palaeoclimate modelling during the
703 Cenozoic. Clim. Past. 12, 1635-1644.
704 Beerling, D.J., Fox, A., Stevenson, D.S., Valdes, P.J., 2011. Enhanced chemistry-climate feedbacks in
705 past greenhouse worlds. P Natl Acad Sci USA 108, 9770-9775.
706 Brass, G.W., Southam, J.R., Peterson, W.H., 1982. Warm Saline Bottom Water in the Ancient Ocean.
707 Nature 296, 620-623.
708 Cramer, B.S., Toggweiler, J.R., Wright, J.D., Katz, M.E., Miller, K.G., 2009. Ocean overturning since the
709 Late Cretaceous: Inferences from a new benthic foraminiferal isotope compilation.
710 Paleoceanography 24.
711 Cramwinckel, M.J., Huber, M., Kocken, I.J., Agnini, C., Bijl, P.K., Bohaty, S.M., Frieling, J., Goldner, A.,
712 Hilgen, F.J., Kip, E.L., Peterse, F., van der Ploeg, R., Rohl, U., Schouten, S., Sluijs, A., 2018.
713 Synchronous tropical and polar temperature evolution in the Eocene. Nature 559, 382-+.
714 Dietmuller, S., Ponater, M., Sausen, R., 2014. Interactive ozone induces a negative feedback in CO2-
715 driven climate change simulations. J. Geophys. Res.-Atmos. 119, 1796-1805.
716 Evans, D., Sagoo, N., Renema, W., Cotton, L.J., Muller, W., Todd, J.A., Saraswati, P.K., Stassen, P.,
717 Ziegler, M., Pearson, P.N., Valdes, P.J., Affek, H.P., 2018. Eocene greenhouse climate revealed by
718 coupled clumped isotope-Mg/Ca thermometry. P Natl Acad Sci USA 115, 1174-1179.
719 Farnsworth, A., Lunt, D.J., O'Brien, C.L., Foster, G.L., Inglis, G.N., Markwick, P., Pancost, R.D.,
720 Robinson, S.A., 2019a. Climate Sensitivity on Geological Timescales Controlled by Nonlinear
721 Feedbacks and Ocean Circulation. Geophys. Res. Lett. 46, 9880-9889.
722 Farnsworth, A., Lunt, D.J., Robinson, S.A., Valdes, P.J., Roberts, W.H.G., Clift, P.D., Markwick, P., Su,
723 T., Wrobel, N., Bragg, F., Kelland, S.J., Pancost, R.D., 2019b. Past East Asian monsoon evolution
724 controlled by paleogeography, not CO2. Sci Adv 5.
725 Foster, G.L., Royer, D.L., Lunt, D.J., 2017. Future climate forcing potentially without precedent in the
726 last 420 million years. Nat Commun 8.
727 Friedrich, O., Norris, R.D., Erbacher, J., 2012. Evolution of middle to Late Cretaceous oceans-A 55
728 m.y. record of Earth's temperature and carbon cycle. Geology 40, 107-110.
729 Gordon, C., Cooper, C., Senior, C.A., Banks, H., Gregory, J.M., Johns, T.C., Mitchell, J.F.B., Wood, R.A.,
730 2000. The simulation of SST, sea ice extents and ocean heat transports in a version of the Hadley
731 Centre coupled model without flux adjustments. Clim. Dyn. 16, 147-168.
732 Gough, D.O., 1981. Solar Interior Structure and Luminosity Variations. Sol Phys 74, 21-34.
733 Gregory, J.M., Ingram, W.J., Palmer, M.A., Jones, G.S., Stott, P.A., Thorpe, R.B., Lowe, J.A., Johns,
734 T.C., Williams, K.D., 2004. A new method for diagnosing radiative forcing and climate sensitivity.
735 Geophys. Res. Lett. 31.
736 Hansen, J., Sato, M., Kharecha, P., Beerling, D., Berner, R., Masson-Delmotte, V., Pagani, M., Raymo,
737 M., Royer, D.L., Zachos, J.C., 2008. Target atmospheric CO2: Where should humanity aim? Open
738 Atmos. Sci. J. 2, 217-231.
739 Hansen, J., Sato, M., Russell, G., Kharecha, P., 2013. Climate sensitivity, sea level and atmospheric
740 carbon dioxide. Philos T R Soc A 371.
741 Hansen, J.E., Sato, M., 2012. Paleoclimate Implications for Human-Made Climate Change. Springer
742 Vienna, Vienna, pp. 21-47.
743 Harris, J., Ashley, A., Otto, S., Valdes, P., Crossley, R., Preston, R., Watson, J., Goodrich, M., Team.,
744 M.P., 2017. Paleogeography and Paleo-Earth Systems in the Modeling of Marine Paleoproductivity: A
745 Prerequisite for the Prediction of Petroleum Source Rocks, in: Mahdi A. AbuAli, I.M., and Hege M.
746 Nordgård Bolås (Ed.), Petroleum Systems Analysis—Case Studies. AAPG Memoir, pp. 27-60.

Climate
of the Past
Discussions

Henkes, G.A., Passey, B.H., Grossman, E.L., Shenton, B.J., Yancey, T.E., Perez-Huerta, A., 2018. Temperature evolution and the oxygen isotope composition of Phanerozoic oceans from carbonate clumped isotope thermometry. Earth Planet. Sci. Lett. 490, 40-50.

Holland, M.M., Bitz, C.M., 2003. Polar amplification of climate change in coupled models. Clim. Dyn. 21, 221-232.

Kennett, J.P., Stott, L.D., 1991. Abrupt Deep-Sea Warming, Palaeoceanographic Changes and Benthic Extinctions at the End of the Paleocene. Nature 353, 225-229.

Kiehl, J.T., Shields, C.A., 2013. Sensitivity of the Palaeocene-Eocene Thermal Maximum climate to cloud properties. Philos T R Soc A 371.

Lunt, D.J., Farnsworth, A., Loptson, C., Foster, G.L., Markwick, P., O'Brien, C.L., Pancost, R.D., Robinson, S.A., Wrobel, N., 2016. Palaeogeographic controls on climate and proxy interpretation. Clim. Past. 12, 1181-1198.

Lunt, D.J., Valdes, P.J., Dunkley Jones, T., Ridgwell, A., Haywood, A.M., Schmidt, D.N., Marsh, R., Maslin, M., 2010. CO2-driven ocean circulation changes as an amplifier of Paleocene-Eocene thermal maximum hydrate destabilization. Geology 38, 875-878.

Murphy, D.P., Thomas, D.J., 2012. Cretaceous deep-water formation in the Indian sector of the Southern Ocean. Paleoceanography 27.

Nowack, P.J., Abraham, N.L., Maycock, A.C., Braesicke, P., Gregory, J.M., Joshi, M.M., Osprey, A., Pyle, J.A., 2015. A large ozone-circulation feedback and its implications for global warming assessments. Nat Clim Change 5, 41-45.

Nunes, F., Norris, R.D., 2006. Abrupt reversal in ocean overturning during the Palaeocene/Eocene warm period. Nature 439, 60-63.

O'Brien, C.L., Robinson, S.A., Pancost, R.D., Damste, J.S.S., Schouten, S., Lunt, D.J., Alsenz, H., Bomemann, A., Bottini, C., Brassell, S.C., Farnsworth, A., Forster, A., Huber, B.T., Inglis, G.N., Jenkyns, H.C., Linnert, C., Littler, K., Markwick, P., McAnena, A., Mutterlose, J., Naafs, B.D.A., Puttmann, W., Sluijs, A., van Helmond, N.A.G.M., Vellekoop, J., Wagner, T., Wrobel, N.E., 2017. Cretaceous sea-surface temperature evolution: Constraints from TEX86 and planktonic foraminiferal oxygen isotopes. 0012-8252 172, 224-247.

Pope, V.D., Gallani, M.L., Rowntree, P.R., Stratton, R.A., 2000. The impact of new physical parametrizations in the Hadley Centre climate model: HadAM3. Clim. Dyn. 16, 123-146.

Poulsen, C.J., Barron, E.J., Arthur, M.A., Peterson, W.H., 2001. Response of the mid-Cretaceous global oceanic circulation to tectonic and CO2 forcings. Paleoceanography 16, 576-592.

Sagoo, N., Valdes, P., Flecker, R., Gregoire, L.J., 2013. The Early Eocene equable climate problem: can perturbations of climate model parameters identify possible solutions? Philos T R Soc A 371.

Scotese, C.R., 2016. PALEOMAP PaleoAtlas for GPlates and the PaleoData Plotter Program, PALEOMAP Project, http://www.earthbyte.org/paleomap-paleoatlas-for-gplates/.

Scotese, C.R., Schettino, A., 2017. Late Permian – Early Jurassic Paleogeography of Western Tethys and the World, in: Soto, J.I., Flinch, J., Tari, G. (Eds.), Permo-Triassic Salt Provinces of Europe, North Africa and the Atlantic Margins. Elsevier, pp. 57-95.

Scotese, C.R., Wright, N., 2018. PALEOMAP Paleodigital Elevation MOdels (PaleoDEMS) for the Phanerozoic, PALEOMAP Project, https://www.earthbyte.org/paleodem-resource-scotese-and-wright-2018/.

Smith, R.S., Gregory, J.M., Osprey, A., 2008. A description of the FAMOUS (version XDBUA) climate model and control run. Geosci Model Dev 1, 53-68.

Song, H.J., Wignall, P.B., Song, H.Y., Dai, X., Chu, D.L., 2019. Seawater Temperature and Dissolved Oxygen over the Past 500 Million Years. J Earth Sci-China 30, 236-243.

Sutton, R.T., Dong, B.W., Gregory, J.M., 2007. Land/sea warming ratio in response to climate change: IPCC AR4 model results and comparison with observations. Geophys. Res. Lett. 34.

Valdes, P.J., Armstrong, E., Badger, M.P.S., Bradshaw, C.D., Bragg, F., Crucifix, M., Davies-Barnard, T., Day, J.J., Farnsworth, A., Gordon, C., Hopcroft, P.O., Kennedy, A.T., Lord, N.S., Lunt, D.J., Marzocchi,

797   A., Parry, L.M., Pope, V., Roberts, W.H.G., Stone, E.J., Tourte, G.J.L., Williams, J.H.T., 2017. The
798   BRIDGE HadCM3 family of climate models: HadCM3@Bristol v1.0. Geosci Model Dev 10, 3715-3743.
799   Verard, C., Hochard, C., Baumgartner, P.O., Stampfli, G.M., 2015. 3D palaeogeographic
800   reconstructions of the Phanerozoic versus sea-level and Sr-ratio variations. J Palaeogeog-English 4,
801   64-84.
802   Witkowski, C.R., Weijers, J.W.H., Blais, B., Schouten, S., Damste, J.S.S., 2018. Molecular fossils from
803   phytoplankton reveal secular Pco_2 trend over the Phanerozoic. Sci Adv 4.
804   You, Y., Huber, M., Muller, R.D., Poulsen, C.J., Ribbe, J., 2009. Simulation of the Middle Miocene
805   Climate Optimum. Geophys. Res. Lett. 36.
806   Zachos, J., Pagani, M., Sloan, L., Thomas, E., Billups, K., 2001. Trends, rhythms, and aberrations in
807   global climate 65 Ma to present. Science 292, 686-693.
808   Zachos, J.C., Dickens, G.R., Zeebe, R.E., 2008. An early Cenozoic perspective on greenhouse warming
809   and carbon-cycle dynamics. Nature 451, 279-283.
810   Zhu, J., Poulsen, C.J., Tierney, J.E., 2019. Simulation of Eocene extreme warmth and high climate
811   sensitivity through cloud feedbacks. Sci Adv 5.

812

813

Table I. List of Paleogeographic Maps and PaleoDEMs

Map Number	Stratigraphic Age Description	Plate Model Age
1	Present-day (Holocene, 0 Ma)	0
2	*Last Glacial Maximum (Pleistocene, 21 ky)**	0
3	*Late Pleistocene (122 ky)**	0
4	*Middle Pleistocene (454 ky)**	0
5	*Early Pleistocene (Calabrian, 1.29 Ma)**	0
6	*Early Pleistocene (Gelasian, 2.19)**	0
7	Late Pliocene (Piacenzian, 3.09)	5
8	*Early Pliocene (Zanclean, 4.47 Ma)**	5
9	*latest Miocene (Messinian, 6.3 Ma)**	5
10	Middle/Late Miocene (Serravallian&Tortonian, 10.5 Ma)	10
11	Middle Miocene (Langhian, 14.9 Ma)	15
12	Early Miocene (Aquitanian&Burdigalian, 19.5 Ma)	20
13	Late Oligocene (Chattian, 25.6 Ma)	25
14	Early Oligocene (Rupelian, 31 Ma)	30
15	Late Eocene (Priabonian, 35.9 Ma)	35
16	late Middle Eocene (Bartonian, 39.5 Ma)	40
17	early Middle Eocene (Lutetian, 44.5 Ma)	45
18	Early Eocene (Ypresian, 51.9 Ma)	50
19	Paleocene/Eocene Boundary (PETM, 56 Ma)	55
20	Paleocene (Danian&Thanetian, 61 Ma)	60
21	KT Boundary (latest Maastrichtian, 66 Ma)	65
22	Late Cretaceous (Maastrichtian, 69 Ma)	70
23	Late Cretaceous (Late Campanian, 75 Ma)	75
24	Late Cretaceous (Early Campanian, 80.8 Ma)	80
25	Late Cretaceous (Santonian&Coniacian, 86.7 Ma)	85
26	Mid-Cretaceous (Turonian , 91.9 Ma)	90

27	Mid-Cretaceous (Cenomanian, 97.2 Ma)	95
28	Early Cretaceous (late Albian, 102.6 Ma)	100
29	Early Cretaceous (middle Albian, 107 Ma)	105
30	Early Cretaceous (early Albian, 111 Ma)	110
31	Early Cretaceous (late Aptian, 115.8 Ma)	115
32	Early Cretaceous (early Aptian, 121.8 Ma)	120
33	Early Cretaceous (Barremian, 127.2 Ma)	125
34	Early Cretaceous (Hauterivian, 131.2 Ma)	130
35	Early Cretaceous (Valanginian, 136.4 Ma)	135
36	Early Cretaceous (Berriasian, 142.4 Ma)	140
37	Jurassic/Cretaceous Boundary (145 Ma)	145
38	Late Jurassic (Tithonian, 148.6 Ma)	150
39	Late Jurassic (Kimmeridgian, 154.7 Ma)	155
40	Late Jurassic (Oxfordian, 160.4 Ma)	160
41	Middle Jurassic (Callovian, 164.8 Ma)	165
42	Middle Jurassic (Bajocian&Bathonian, 168.2)	170
43	Middle Jurassic (Aalenian, 172.2 Ma)	175
44	Early Jurassic (Toarcian, 178.4 Ma)	180
45	Early Jurassic (Pliensbachian, 186.8 Ma)	185
46	Early Jurassic (Sinemurian/Pliensbachian, 190.8 Ma)	190
47	Early Jurassic (Hettangian&Sinemurian, 196 Ma)	195
48	Late Triassic (Rhaetian/Hettangian, 201.3 Ma)	200
49	Late Triassic (Rhaetian, 204.9 Ma)	205
50	Late Triassic (late Norian, 213.2 Ma)	210
51	Late Triassic (mid Norian, 217.8 Ma)	215
52	Late Triassic (early Norian, 222.4 Ma)	220
53	Late Triassic (Carnian/Norian 227 Ma)	225
54	Late Triassic (Carnian, 232 Ma)	230

55	Late Triassic (early Carnian, 233.6)	235
56	Middle Triassic (Ladinian, 239.5 Ma)	240
57	Middle Triassic (Anisian, 244.6 Ma)	245
58	Permo-Triassic Boundary (252 Ma)	250
59	Late Permian (Lopingian, 256 Ma)	255
60	late Middle Permian (Capitanian, 262.5 Ma)	260
61	Middle Permian (Wordian/Capitanian Boundary 265.1 Ma)	265
62	Middle Permian (Roadian&Wordian, 268.7 Ma)	270
63	Early Permian (late Kungurian, 275 Ma)	275
64	Early Permian (early Kungurian, 280 Ma)	280
65	Early Permian (Artinskian, 286.8 Ma)	285
66	Early Permian (Sakmarian, 292.6 Ma)	290
67	Early Permian (Asselian, 297 Ma)	295
68	Late Pennsylvanian (Gzhelian, 301.3 Ma)	300
69	Late Pennsylvanian (Kasimovian, 305.4 Ma)	305
70	Middle Pennsylvanian (Moscovian, 311.1 Ma)	310
71	Early/Middle Carboniferous (Baskirian/Moscovian boundary, 314.6 Ma)	315
72	Early Pennsylvanian (Bashkirian, 319.2 Ma)	320
73	Late Mississippian (Serpukhovian, 327 Ma)	325
74	Late Mississippian (Visean/Serpukhovian boundary, 330.9 Ma)	330
75	Middle Mississippian (late Visean, 333 Ma)	335
76	Middle Mississippian (middle Visean, 338.8Ma)	340
77	Middle Mississippian (early Visean, 344 Ma)	345
78	Early Mississippian (late Tournaisian, 349 Ma)	350
79	Early Mississippian (early Tournaisian, 354Ma)	355
80	Devono-Carboniferous Boundary (358.9 Ma)	360
81	Late Devonian (middle Famennian, 365.6 Ma)	365

82	Late Devonian (early Famennian, 370 Ma)	370
83	Late Devonian (late Frasnian, 375 Ma)	375
84	Late Devonian (early Frasnian, 380 Ma)	380
85	Middle Devonian (Givetian, 385.2 Ma)	385
86	Middle Devonian (Eifelian, 390.5 Ma)	390
87	Early Devonian (late Emsian, 395 Ma)	395
88	Early Devonian (middle Emsian, 400 Ma)	400
89	Early Devonian (early Emsian, 405 Ma)	405
90	Early Devonian (Pragian, 409.2 Ma)	410
91	Early Devonian (Lochkovian, 415 Ma)	415
92	Late Silurian (Pridoli, 421.1 Ma)	420
93	Late Silurian (Ludlow, 425.2 Ma)	425
94	Middle Silurian (Wenlock, 430.4 Ma)	430
95	Early Silurian (late Llandovery, 436 Ma)	435
96	Early Silurian (early Llandovery, 441.2 Ma)	440
97	Late Ordovician (Hirnantian, 444.5 Ma)	445
98	Late Ordovician (Katian, 449.1 Ma)	450
99	Late Ordovician (Sandbian, 455.7 Ma)	455
100	Middle Ordovician (late Darwillian,460 Ma)	460
101	Middle Ordovician (early Darwillian,465 Ma)	465
102	Early Ordovician (Floian/Dapingianboundary, 470 Ma)	470
103	Early Ordovician (late Early Floian, 475 Ma)	475
104	Early Ordovician (Tremadoc, 481.6 Ma)	480
105	Cambro-Ordovician Boundary (485.4 Ma)	485
106	Late Cambrian (Jiangshanian, 491.8 Ma)	490
107	Late Cambrian (Pabian, 495.5 Ma)	495
108	late Middle Cambrian (Guzhangian, 498.8 Ma)	500
109	late Middle Cambrian (early Epoch 3, 505 Ma)	505

110	early Middle Cambrian (late Epoch 2, 510 Ma)	510
111	early Middle Cambrian (middle Epoch 2, 515 Ma)	515
112	Early/Middle Cambrian boundary (520 Ma)	520
113	Early Cambrian (late Terreneuvian, 525 Ma)	525
114	Early Cambrian (middle Terreneuvian, 530 Ma)	530
115	Early Cambrian (early Terreneuvian, 535 Ma)	535
116	Cambrian/Precambrian boundary (541 Ma)	540

814 * *Simulations were not run for the time intervals highlighted in italics.*

815

816